Article

Influence of pore networking and electric current density on the crack pattern in reinforced concrete test due to pressure rust layer at early ages of an accelerated corrosion test

Ángela M. Bazán , Encarnación Reyes and Jaime C. Gálvez *

Departamento de Ingeniería Civil: Construcción, E.T.S de Ingenieros de Caminos, Canales y Puertos, Universidad Politécnica de Madrid. C / Profesor Aranguren, s/n, 28040, Madrid. Spain.; email: angela.moreno@upm.es (A.M.B.), Encarnacion.reyes@upm.es (E.R.), jaime.galvez@upm.es (J.C.G)

* Correspondence: jaime.galvez@upm.es; Tel.: +34-910674125 (J.C.G.)

Abstract: Research on early stages of corrosion of steel bars, together with the formation and development of cracks induced in the surrounding concrete and caused by chloride penetration, is relevant in improving the durability of reinforced concrete structures. This paper uses integration of the analytical models examined in the published literature, combined with experimental research in corrosion induced at the concrete/steel interface, in estimating the time-to-crack initiation of reinforced concrete subjected to corrosion. This work studies the influence of the porous network and electric current density on the cracking process at early ages. The experimental campaign was performed by using an accelerated corrosion test on a conventional concrete (CC) and a concrete with silica fume (SFC) by submitting them to a current density of $50\mu A/cm^2$ and $100\mu A/cm^2$. Examination performed by scanning electron microscopy (SEM) and energy-dispersive X-ray spectroscopy (EDS) provided both qualitative and quantitative information on the penetration of the rust layer in the surrounding concrete porous network. Strain gauges were used to measure corrosion-induced deformations between steel and concrete matrices, as well as the formation of corrosion-induced cracks. A good correlation between the rate of penetration of the rust products in the surrounding pores   and the delay of the cracking pressure in concrete was observed from the experimental results. This phenomenon is incorporated into the analytical model by using a reduction factor, which mainly depends on the pore size of the concrete. The crack width obtained exhibited a significant dependency on electric current density at the beginning of the test, depending mainly on the pore size of the concrete later.

1. Introduction

Durability of reinforced concrete is a significant research line, given the high costs associated with the maintenance and repair of structures. Corrosion of steel reinforcement is one of the most serious and frequent   deterioration mechanisms identified in reinforced concrete structures. This deterioration process frequently causes significant structural problems that eventually lead to collapse [1, 2]. Steel embedded in normal reinforced concrete is protected from corrosion due to a passive film, formed on the surface of the steel because of the high alkalinity of pore solution in the concrete. The break of the passive barrier would occur with the pH value being lower than 10 or, most commonly, by the presence of chloride ion.

Once the passive film is broken, corrosion starts and rust products are produced by an electrochemical reaction of the iron. The rust produced occupies a larger volume than the original

material. At an early stage this extra volume can be accommodated by a region of the porous network of the concrete that surrounds the rebar, delaying the tensile stress development in the concrete/steel interface [3, 4]. Therefore, this region of concrete, called the corrosion accommodation region (CAR), has a major influence on the prediction of the crack initiation time and crack propagation [4-6].

The CAR thickness depends on several factors, in particular the volume and connectivity of the pores in the concrete/steel interface and the corrosion current density. The microstructural characteristics of the concrete/steel interface, in turn, depend on the surface area of reinforcement, w/c ratio, degree of hydration, degree of consolidation and, among others, type of cement. Thus, accurate prediction of the CAR size and crack initiation time is highly complex. Several published authors have proposed a fixed value for the CAR thickness which due to expansive pressure must be filled with corrosion products before tension stress development [5, 7]. Recent works have examined the formation and propagation of corrosion-induced cracks and the CAR size by using the X-ray attenuation technique [4, 8].

Once the CAR is filled, the corrosion products cause expansive pressure on the surrounding concrete, with tensile stresses emerging on the concrete/steel interface [5]. Eventually, this can lead to cracking in the case of the tensile stresses exceeding the tensile strength of the concrete [9].

The formation of cracks provides a path through which the aggressive agents from the environment can easily penetrate and reach the reinforcement, accelerating the corrosion process. In this stage the corrosion products begin to fill the cracks, which then causes crack opening and propagation, spalling and delamination of the cover [10, 11]. Figure 1 shows the three main stages of the corrosion process.
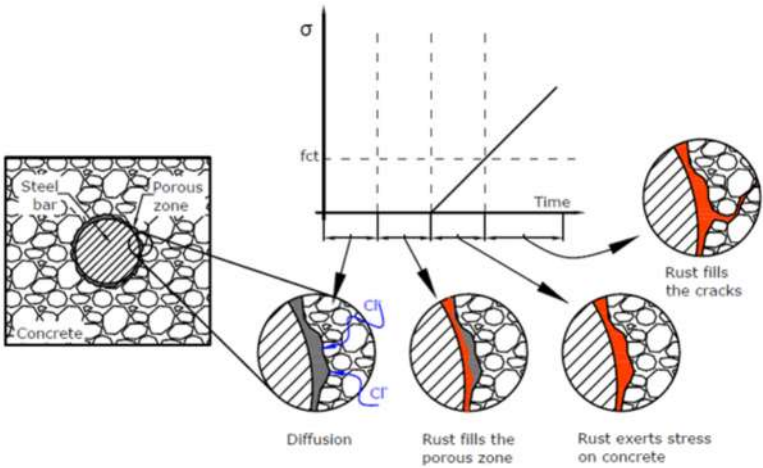
Figure 1. Corrosion cracking process: the three-stage-model.

In order to predict time-to-crack initiation, the propagation period and ultimately service life of reinforced structures in chloride environments, it is necessary to obtain a thorough understanding of the corrosion process from its beginning, studying in detail the CAR formation. Many of the experimental studies on corrosion-induced crack initiation and propagation conducted previously have used high corrosion rates to accelerate the process on concrete with embedded rebar specimens being monitored with strain gauges on the surface [12, 13]. Some authors have used microscopic techniques to study the concrete/steel interface [14]. The authors of this paper propose combining both experimental methods by using strain gauges placed as closely as possible to the rebar to assess the radial displacement of the surrounding concrete and scanning electron microscopy (SEM), along with energy-dispersive X-ray spectroscopy (EDS) to examine the concrete/steel interface. This combined method exhibited an adequate performance to study the corrosion process from the earliest stages in a previous published work [15]. In this paper, however, results of an experimental work conducted to investigate the influence of the pore size and corrosion current density on the CAR and cracking process by using the proposed procedure are presented. The experimental campaign used accelerated corrosion tests with densities of $50\mu A/cm^2$ and $100\mu A/cm^2$ [4, 13, 16-18] on two high-

83   strength concretes: one without admixtures and another with silica fume (SF). The objective of using
84   SF in one mixture was to obtain two concretes with distinct microstructures in order to study the
85   influence of the porous network on the CAR as well as the formation and propagation of corrosion-
86   induced cracks. The specimens used had a steel rebar embedded in the middle. The strain of the
87   concrete due to corrosion of the rebar was monitored by means of strain gauges. The aforementioned
88   SEM and EDS were used to examine the penetration of the rust corrosion products found in the
89   concrete. Lastly, the paper uses an analytical model based on the thick-walled cylinder approach [11]
90   to reproduce the experimental results. The crack width is predicted by using a combination of
91   wavelength dispersive spectroscopy along an analytical line that covers the interface and the radial
92   displacement assessed by the gauges. Furthermore, the crack initiation time is estimated from
93   converting the retrieved strain data into stresses and by comparing them with the tensile strength.

94   **2. Experimental campaign**

95   *2.1 Materials, mix proportioning and specimens*

96   Two concrete mixtures were designed to obtain similar properties, though with a different pore
97   microstructure. Portland cement CEM I 52.5 R and Portland cement CEM I 42.5 R, in accordance with
98   the standard EN 197-1:2011, were used for the preparation of a conventional concrete (CC) without
99   admixtures and the earlier mentioned SFC with SF as a mineral admixture. The second mixture uses
100   SF with 10% of replacement percentage weight of cement and two as an efficiency factor. The
101   water/binder ratio was 0.45 in both cases. Chlorides were added to the mix in order to generate
102   depassivation of the steel [6, 19]. To this end, 3% of $CaCl_2$ by weight of cement was added to each
103   concrete [6, 19, 20]. Furthermore, a polycarboxylate-based superplasticizer (SP), named Sika
104   ViscoCrete 5720, was added to improve workability. Mix proportioning is shown in Table 1.
105

106   **Table 1.** Mix proportioning.

Mix	Water/binder ratio	Binder (kg/m³)		Aggregate (kg/m³)			Admixture (% binder weight)	
		Cement	Silica fume	Gravel	Grit	Sand	Superplasticizer	CaCl2
CC	0.45	350	-	552.2	225.4	907.8	0.9	3
SFC	0.45	280	35*	552.2	225.4	907.8	1	3

107   *Efficiency factor of silica fume is taken 2

108   In order to study the evolution of the corrosion products at different ages from early stages and
109   with two current densities, 16 specimens of reinforced concrete were cast for each concrete type with
110   the following dimensions: 15 x 15 x 15 cm³. Rebars of diameter of 20 mm were treated with the aim
111   of protecting the steel from corrosion initiators, propagating points and preferential attacks. First,
112   rebars were coated entirely with epoxy resin. Later, the rebars were machined and the diameter
113   reduced by up to 12 mm along 100 mm, beginning at a point located 30 mm from the extreme of the
114   specimen, as shown in Figure 2.

115
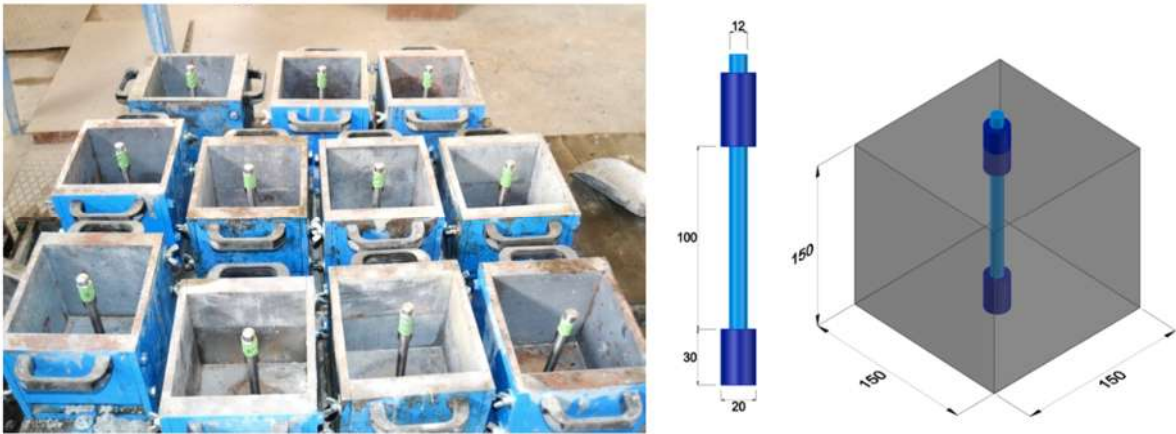
116   **Figure 2**. Details of the bars in the moulds before casting: a) photo of the moulds, b) sketch of the
117   specimen. (Dimensions in mm).

118   With the objective of monitoring the radial displacement of the surrounding concrete induced
119   by the corrosion, strain gauges were embedded in three specimens per concrete type and current
120   density. For such a purpose, these specimens were cast in two stages, casting one half of the volumes
121   in each of them. When the first half was set, four strain gauges were placed perpendicularly to each
122   other at the concrete surface around the steel rebar as closely as possible [21]. A resin appropriate for
123   monitoring purposes was used to glue the strain gauges. Lastly, a single component solvent-based
124   polyurethane lacquer, PU140, was used as protective film on the gauge, in order to avoid any
125   potential problem derived from the elevation of the humidity caused by the casting of the second
126   half. Figure 3 shows the position of the strain gauges around the rebar. Table 2 shows the
127   characteristics of the strain gauges used in this work.

128
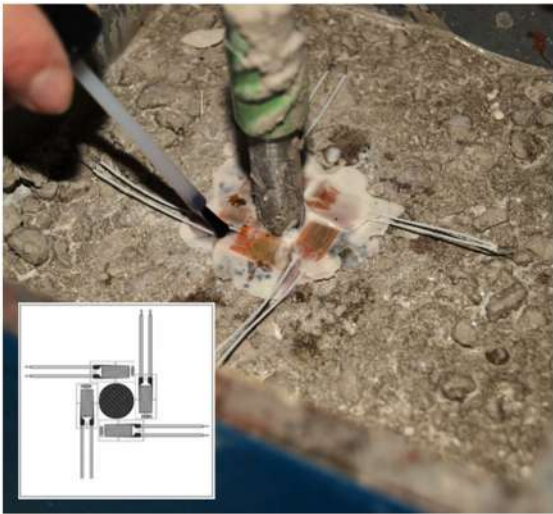
129   **Figure 3.** Bonding of the strain gauges before the accelerated corrosion testing.

130   **Table 2.** Strain gauge characteristics.

Type HBM	Operating temperature range compensated (ºC)	Resistance (Ω)	Gauge factor	Dimensions (mm)	
				Measuring grid	Measuring grid carrier
K-CLY4-0100-1-120-O	-10/ +45	120 ± 0.35 %	2.07 ± 1.0 %	10 x 5	8 x 18

131

132   *2.2 Mechanical test*

133   Four experimental tests were carried out in order to study the mechanical properties of the
134   concrete. The compressive strength, the elastic modulus and the tensile strength were measured at
135   28 days on cylindrical ϕ150x300mm specimens. Compression tests were carried out to obtain the
136   compressive strength in accordance with EN 12390-3 by using three specimens for each concrete type.
137   The elastic modulus was estimated in accordance with standard EN 12390-13. The indirect tensile
138   strength was obtained according to standard EN 12390-6 by a tensile splitting test on three specimens.
139   Lastly, fracture behaviour tests in accordance with the recommendation RILEM TC-187 SOC
140   were carried out to complete the mechanical characterisation of the concretes. In order to measure
141   the specific fracture energy, three-point bending tests were performed on three concrete beams for
142   each type of mixture. The dimensions of the specimens were 100x100x430mm^3 with a notch at the
143   centre of 1/3 of the height of the beam. The mechanical properties of the two concretes studied are
144   showed in Table 3.

145   **Table 3.** Mechanical properties.

	Compressive strength f_c (MPa)	Elasticity modulus E (GPa)	Tensile strength f_{ct} (MPa)	Fracture energy G (N/m)
SFC	62.38	31.89	4.03	179.6
CC	65.91	33.97	4.98	172.7

146   *2.3   Accelerated corrosion tests and test programme*

147   The experimental set-up used is shown in Figure 4. The concrete-rebar system was externally
148 short-circuited. A constant anodic current was applied to enforced corrosion. The electric circuit
149 joined the steel rebar, the anode, with a lead sheet being placed on the surface of the slabs which
150 acted as a cathode. The electrical connection was performed by partially immersing the specimens in
151 tap water. The water level was maintained at approximately 1cm height. In order to induce corrosion,
152 3% of $CaCl_2$ by weight of cement was added to the mix [16].

153
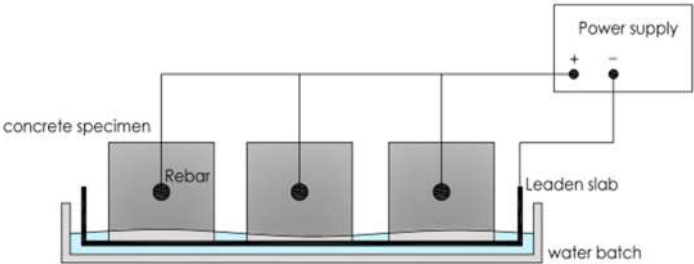
154   **Figure 4.** Scheme of accelerated corrosion test.

155   In this study, specimens were subjected to current densities of 50 and 100 µA/cm2 in order to
156 examine the influence of velocity of corrosion in the CAR formation. These values allow a sufficiently
157 short experiment, but keep induced corrosion within values which might be found in practice [16].
158 With such an objective, the intensity density must stay somewhat low (< 200 µA/cm²) with respect to
159 Faraday's law, otherwise a significant increase of in the tension-strain response and, consequently, in
160 the cracking process might occur. Theoretically, intensity densities could reach 500µA/cm², but non-
161 negligible variations might appear and the accuracy of the experiment could not be guaranteed [17].
162   Two independent circuits were assembled: the first one comprised only the specimen with strain
163 gauges; and the second one the rest of the specimens by using a parallel system. Specimens from the
164 second circuit were disconnected and extracted at different ages in order to provide study by means
165 of SEM. Since a constant current density of 50 and 100µA/cm² was assumed, the total current in each
166 circuit could be computed. Results of the surface rebar electricity density and total electricity current
167 in each circuit are shown in Table 4.

168

169   **Table 4.** Surface rebars electricity density and total electricity current in the specimens.

Number of specimens	Surface rebar (cm²)	Current density (µA/cm²)	Total current/circuit (mA)
8	37.7	50	1.9
		100	3.8

170   *2.4 Microscope Analysis*

171   The study of the evolution of the corrosion process and growth of the rust corrosion layer (CL)
172 were observed and analysed by means of SEM and EDS. The specimens were disconnected and cut
173 at the following ages: one, two, five, eight, 14, 21, 26 and 35 days. First, prismatic samples containing

174 the rebar with a square base of 50x50 mm² were cut. Then, thin slices of approximately 1 mm were
175 obtained for SEM observation. To this end, the samples were inserted in a vacuum chamber until
176 constant weight, and then impregnated with a low-viscosity epoxy resin. The resin was hardened for
177 48 hours. At a later stage, all the samples were polished by using a lapping and polishing machine
178 with silicon carbide abrasive papers from grades 240 to 1200 lubricated with water. Polishing was
179 performed by using Wenol® metal polish to improve imaging quality. Lastly, a sputter conductive
180 coating of carbon was applied to the polished area in order to obtain a higher resolution image,
181 allowing a more detailed examination.

182 A field-emission scanning electron microscope (JEOL Superprobe JXA-8900 M) and operated in
183 backscattered electron (BSE) mode was used to create the element maps of the steel/concrete interface
184 at different ages. On this basis the time-dependent corrosion product development, the CAR and
185 subsequent formation and propagation of cracks were studied. Four chemical elements were
186 analysed to examine rust development on the concrete/steel interface: calcium, iron, oxygen and
187 silicon. The results are represented in one general image. Different colour intensities, ranging from
188 black over green to purple, make observation of layers in each element map possible. Steel rebars and
189 the corrosion layer are brighter in the images due to the oxygen content. In the case of concrete, Ca
190 and Si are found. An analytical line was selected across the steel/concrete interface on each image.
191 The size of the reference region of each image depended on the age. Boundary conditions are shown
192 in Table 5.

193   **Table 5.** Boundary conditions of wavelength dispersive X-ray spectroscopy (WDS).

	Element map				Analytical line	
Days	Size (pixel)	Size pixel (μm)	Dual time (ms)	Accelerating voltage (kV)	Length (μm)	Interval (μm)
1-14	400x400	0.5	15	20	200-250	15
26	600x600	0.5	15	20	250-300	15
35	600x600	0.5	15	20	300-600	15

194 *2.5 Pore size*

195 Figure 5 shows frequency distribution of the pores for the mixtures studied and the distribution
196 of macro and micropores for the SFC and the high-strength concrete without any additions (CC) at
197 28 days of curing. In this work, macropores are considered as those with a diameter greater than 50
198 nm in width according to IUPAC [22]. Table 6 shows the percentage of total porosity, the average
199 pore diameter and the median pore diameter for each concrete.
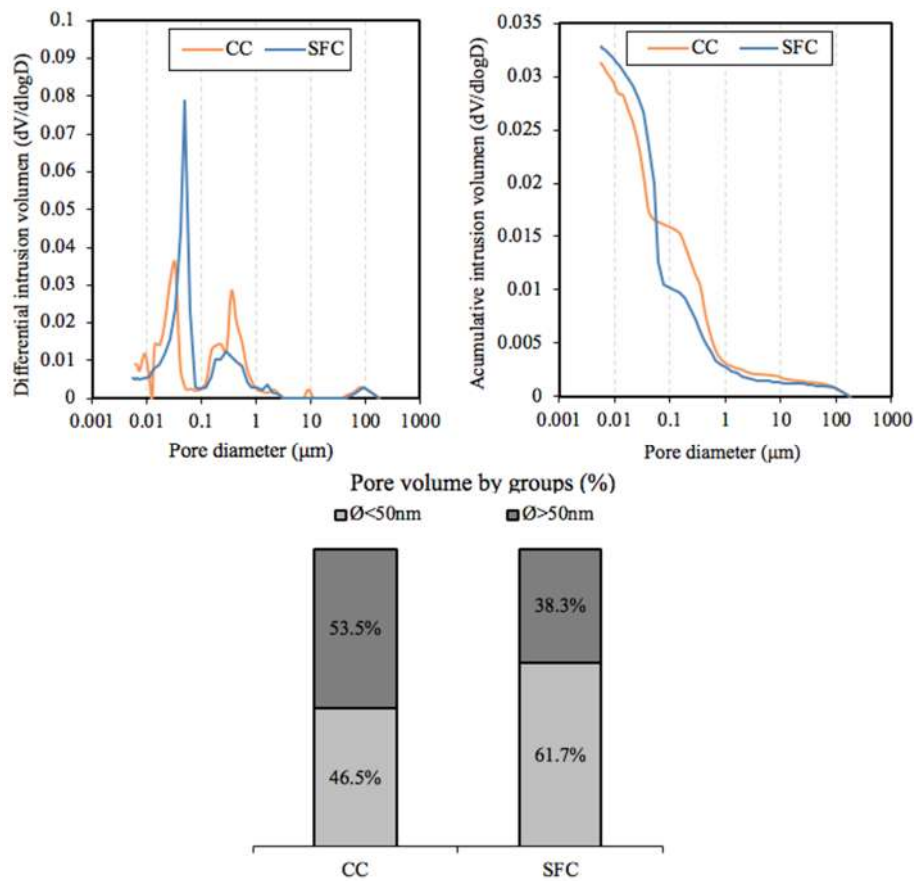
Figure 5. Pore size distribution for each concrete (SFC, silica fume concrete and CC, conventional concrete).

Table 6. Total porosity and effective capillary porosity for each concrete (SFC, silica fume concrete and CC, conventional concrete).

	CC	SFC
Porosity (%)	7.39	7.55
Average pore diameter (μm)	0.036	0.029
Median pore diameter (μm)	0.12	0.06

This work sought the influence of the pore size by maintaining the rest of the properties relatively constant. As Table 6 shows, the total porosity is quite similar in each concrete. Nevertheless, the average pore diameter and the median pore diameter are significantly higher in CC in comparison with SFC. Figure 5 shows the distribution of macro and micropores in each concrete, with a significantly higher amount of micropores being observed in SFC in comparison with the conventional concrete. Therefore, the concrete with silica fume has a denser network and a smaller average pore diameter, while presenting a similar overall porosity. The median pore diameter of SFC is half that of the pore diameter of CC. The general smaller diameter of the pores in SFC in comparison with CC could have a notable influence on a less accommodating capacity of the rust products.

3. Results

3.1 Experimental displacement field measurements at steel/concrete interface with strain gauges

217   The strain gauges were placed as closely as possible to the steel rebar in order to measure the
218 strain as the rust products were growing. The data were checked daily and recorded. Figure 6 shows
219 the circumferential strain around the rebar versus time for each concrete type and density. The value
220 corresponds to the average circumferential strain measured by the embedded gauges in two
221 specimens for each case studied.

222
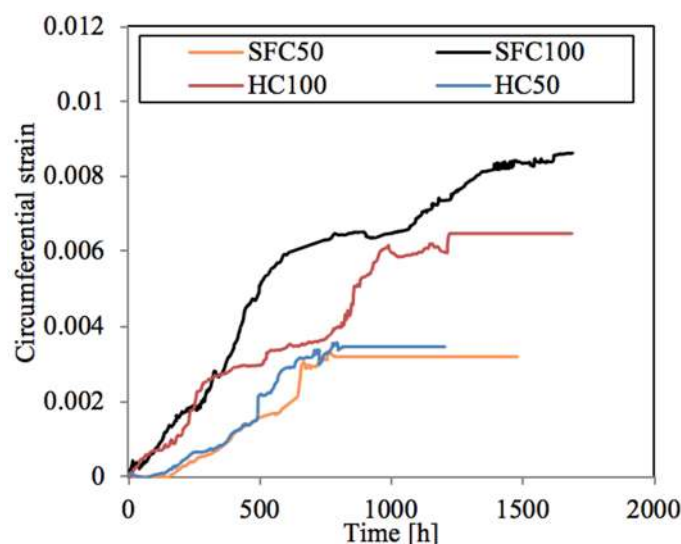
223   **Figure 6.** Circumferential strain around the rebar versus time for each concrete type and current
224   density.

225   Based on the circumferential strain shown in Figure 6, the time of significant increment of the
226 tension stress initiation on the concrete/steel interface may be estimated. The results obtained for
227 $100\mu A/cm^2$ show a linear pattern from the very beginning. In the case of the radial stresses with
228 $50\mu A/cm^2$, a bilinear pattern may be approached. Therefore, in this case the strain gauges did not
229 measure strain over a period of time, corresponding with the formation of the CAR. The time needed
230 to accommodate the rust products (the horizontal part) is quite similar, around 120 hours, in each
231 specimen. Once the CAR was completely filled with rust products, expansive pressure started with
232 a linear increment.

233 *3.2 Microstructure characteristics*

234

235   Mapping was adopted to observe the development of corrosion products at the steel/concrete
236 interface. The areas with high levels of Fe are shown in purple and the rust layer represented in green.
237 In order to complement the study, the distributions of corrosion products were analysed by
238 EDS/WDS along an analytical line. Four chemical elements were chosen for this analysis: Fe, O, Si
239 and Ca. Depending on the availability of these elements, the three main layers involved in the
240 corrosion process could be distinguished: steel, millscale (CL+CAR) and concrete. As an example,
241 Figure 7 shows the amount of Fe at eight, 14 and 35 days for the CC mixture under a current density
242 of $50\mu A/cm^2$ by using the colour code. In the right graphs, the distributions of Fe, O, Si and Ca are
243 shown. The horizontal axis represents the distance from the starting point of the analytical line and
244 the vertical axis the counts of photoelectrons per second.
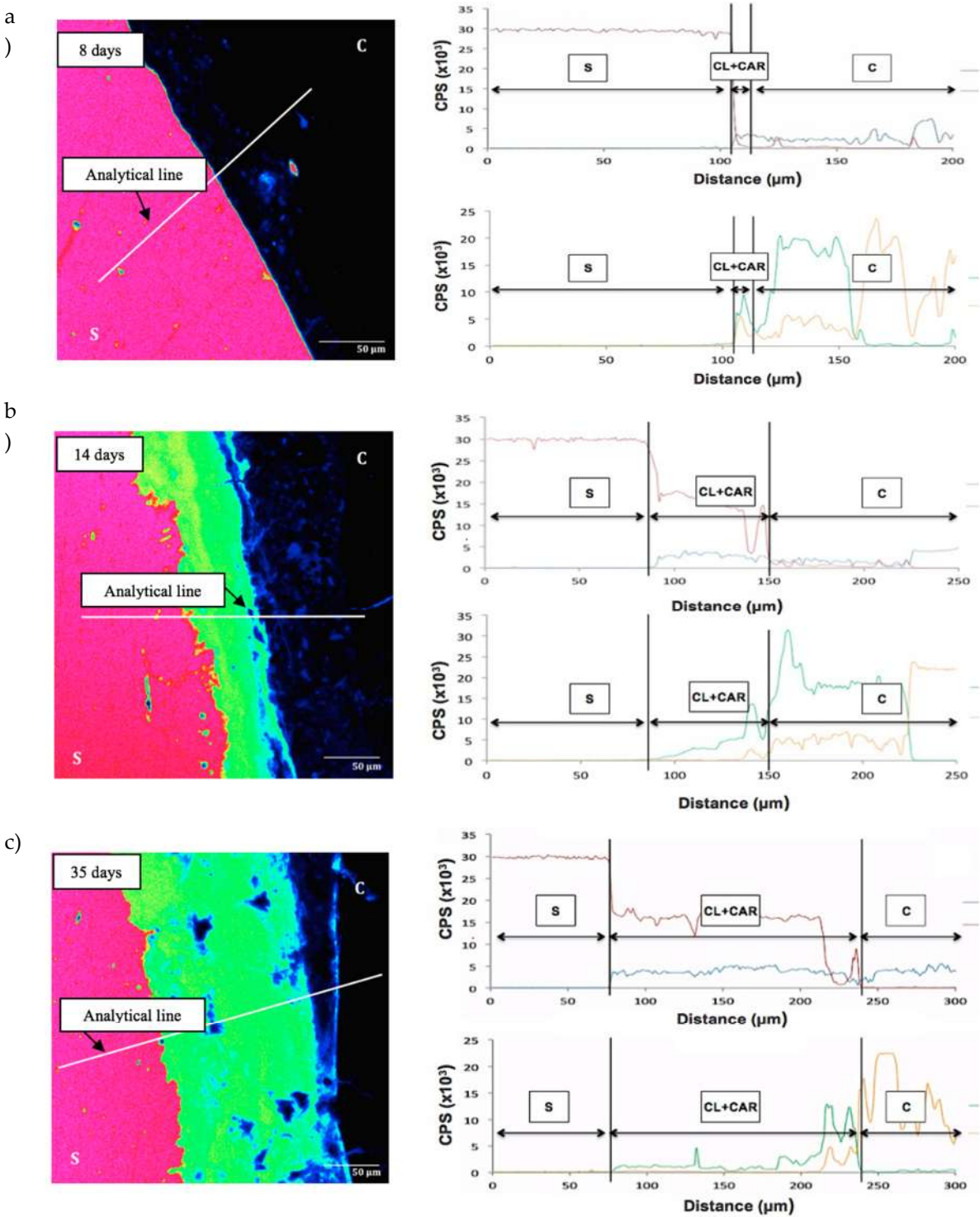
Figure 7. BSE image at the steel/concrete interface (C, concrete; CL+CAR, Millscale; S, Steel) and analytical lines across the interface of CC at a) 8 days, b) 14 days and c) 35 days with a density current of 50µA/cm². Upper curves of each age: Fe and O; bottom curves of each age: Si and Ca

In the image corresponding to 35 days the end of the filling of the ΔR can be distinguished. This specimen had a rust layer (CL) of 18µm and a layer where corrosion products were diffusely distributed (CAR). Some authors refer to this as the 'corrosion filled paste' [23, 24] when describing a two-step process in the corrosion distribution. This indicates that a corrosion layer is first formed around the steel rebar which then penetrates through the concrete. Based on these results, the millscale (CL+CAR) thickness of the rust products can be determined in all the cases at 100 µA/cm²

255 and 50 μA/cm². As Figure 8 shows, the current intensity and the type of concrete had a considerable
256 effect on the millscale thickness at the same age (14 days).

257 (SFC50)   (SFC100)   (CC50)   (CC100)
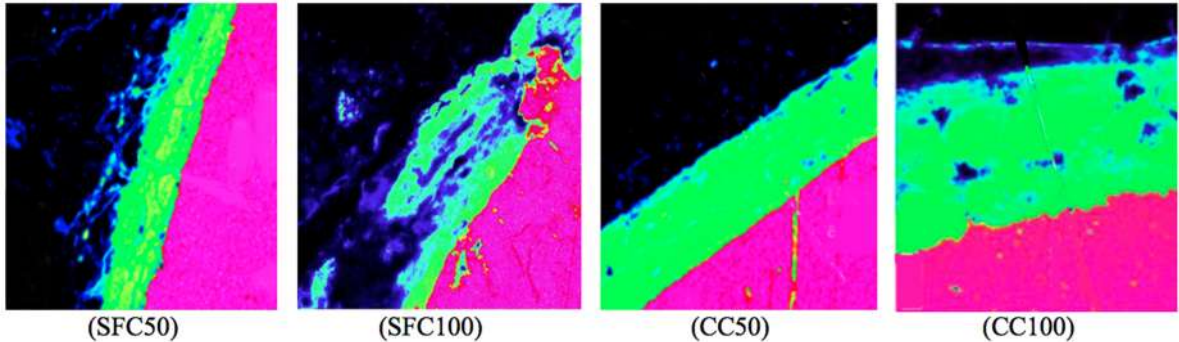
258 **Figure 8**. BSE image at the steel (purple)/concrete(black) interface at 14 days for each concrete (SFC,
259 silica fume concrete and CC, conventional concrete) at at 100 μA/cm² and 50 μA/cm².

260 Table 7 shows the evolution of the corrosion in time, where the values of the millscale thickness
261 (ΛR) as a function of time are collected. On the basis of these values, it could be concluded that for
262 the first 120 hours no significant increase in millscale thickness was detected in the specimens under
263 a current density of 50μA/cm². Afterwards, a linear growth could be appreciated.

264 **Table 7.** Thickness of the millscale as a function of the time, for the specimens of SFC and CC with a
265 density current of 50 and 100μA/cm².

Tiempo (h)	ΔR (μm)			
	SFC50	SFC100	CC50	CC100
24.00	0	0	0	0
48.00	0	0	0	20
120.00	5	18	4	35
192.00	7	42	18	65
336.00	22	85	43	130
624.00	72	215	125	180
840.00	115	255	170	225

266
267 Although examination of the concretes studied has not shown significant change in total
268 porosity, a considerable pore refinement has been obtained by adding silica fume. SFC presented a
269 reduction of 15.2% in the percentage of macropores, increasing the percentage of micropores with
270 regard to CC. This might explain the differences obtained in the corrosion layer development, even
271 though the variation exhibited between different concretes and intensities was relatively small.

4. Discussion

273 In order to compare the behaviour of the four cases studied with two current densities and two
274 concrete types, the difference in current density used in the test of the circumferential strain
275 development had to be eliminated. This could be achieved by multiplying the time by intensity. The
276 specimens subjected to a current density of 100μA/cm² corresponded to a total current of 3.77 mA
277 applied. The specimens under 50μA/cm² were subjected to a total current of 1.89 mA. Figure 9 shows
278 the circumferential strain measured by the gauges in the vertical axis versus the total electric charge
279 applied to each concrete in the horizontal one. As can be observed, curves corresponding to the lowest
280 current density exhibited a bilinear pattern. Both concrete types needed around 500 C, and thus a
281 similar time range, to induce notable pressure and therefore circumferential strain. After this turning
282 point, at around 500 C, each concrete showed a linear pattern. The regression line for this part is the
283 same for both concrete mixtures, with a quite good R^2 coefficient. In the case of the highest current
284 density, each concrete exhibited a linear pattern of the circumferential strain, and thus the

285   circumferential stress, from the beginning. In this case, the regression line is similar for each concrete
286   mixture and the slope slightly lower than the regression line corresponding to SFC50 and CC50.
287   The regression coefficient R^2 obtained for SFC100 is considerably worse than that obtained in
288   other cases. This might have been caused by the breaking of three of the four gauges used in the
289   measurement of the circumferential strain in this case, as shown in Figure 10.
290   The results show that the placement of the four gauges around the steel bar might offer an
291   improvement for cracking models versus those where they are placed on the concrete surface. The
292   data acquired are in general a good representation for the development of stress throughout the
293   corrosion process.

294
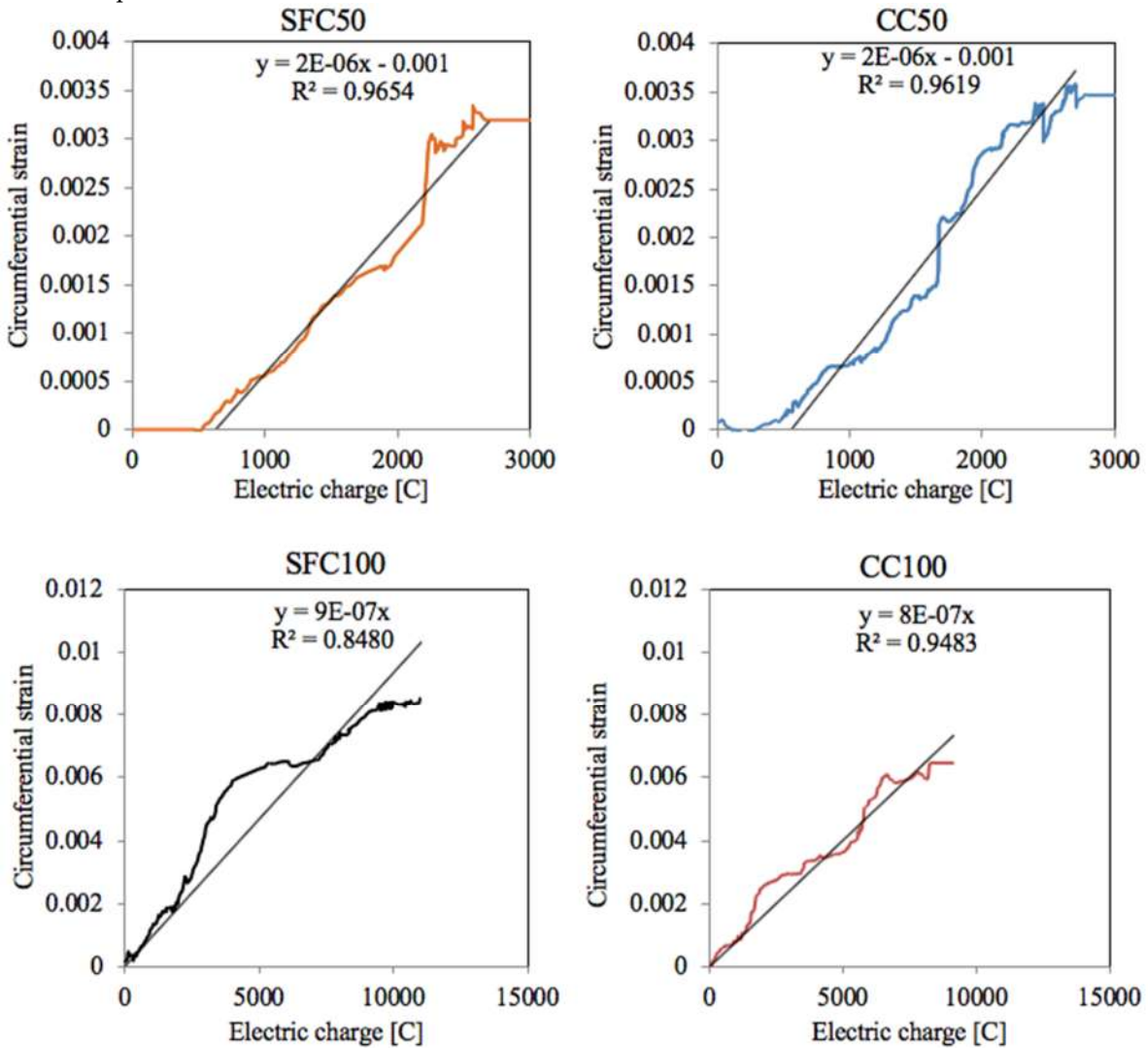
295   **Figure 9.** Evolution of the circumferential strain as a function of the electric charge for each specimen
296   at 50 and 100µA/cm².

297
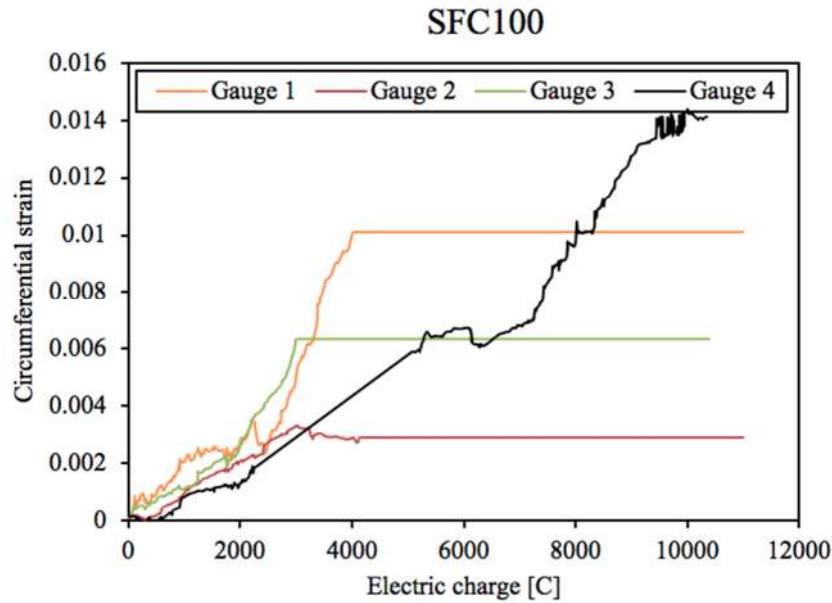
Figure 10. Evolution of the circumferential strain as a function of the electric charge measured by the four gauges for SFC 100.

Figure 11 shows the experimental circumferential strain as a function of the rust layer thickness during the corrosion process and the regression line obtained. As can be seen, all cases presented a linear regression with a good R^2 coefficient. The slope of the regression line was the same for each concrete at different current intensities and only slightly lower for CC mixtures in comparison with SFC mixtures. The rapid development of the corrosion process in SFC100 mixture, together with the smaller average pore diameter size in comparison with the conventional mixture, cause a lower capability to accommodate the corrosion products, producing larger circumferential deformations than other cases from the beginning.
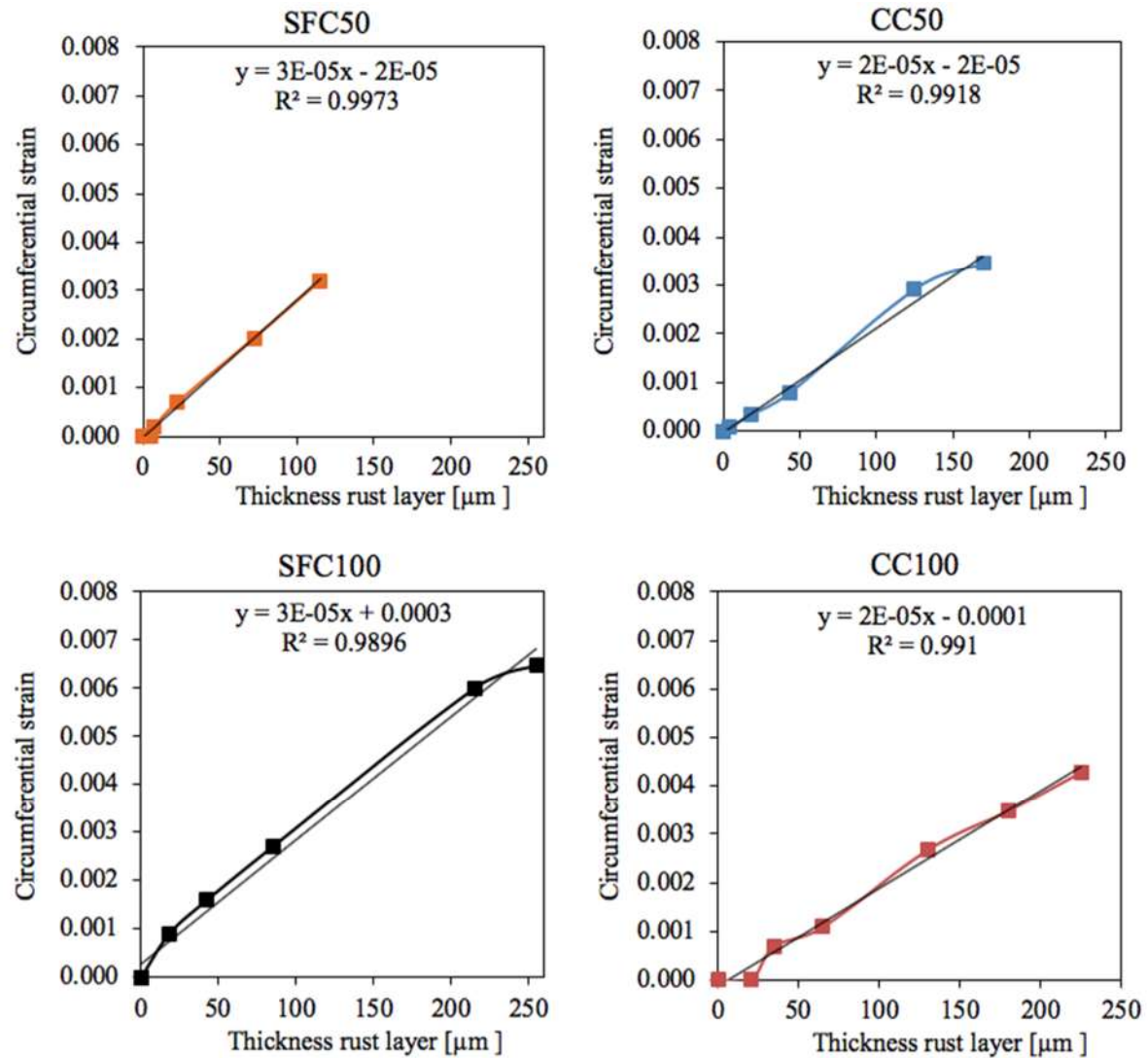
309　**Figure 11**. Evolution of the circumferential strain as a function of the rust layer thickness for both
310　concretes at 50 and 100μA/cm².

311　**5. Analytical verification**

312　　Much published research has offered analytical models that describe the cracking process based
313　on a thick-walled cylinder of one or two layers in line with the theory of plasticity proposed by
314　Timoshenko and Goodier [25]. The most commonly used model today is described by Den Ujil and
315　Bigaj [26], who proposed a model based on Tepfers' theory on the relationship between radial
316　displacement and radial compression stress at the interface steel/concrete (Eq. 1) and circumferential
317　hoop strains by using the confining capacity of concrete.

$$\frac{\Delta R}{r} + \frac{n\,w}{2\pi\,r} = \epsilon \tag{1}$$

318　　Where, w is the width of crack, r is the radius, ΔR is the radial displacement, n is the number of
319　cracks and ε is the circumferential strain, including the opening of the cracks.
320　　Recently, some authors have proposed that the three-stage model should be modified into a two-
321　stage model [27]. In line with such an approach, the penetration of rust products into the porous
322　microstructure and formation of a corrosion layer at the interface might occur simultaneously once
323　the steel corrosion has been initiated. Based on such rationale, in this work the CAR and CL have
324　been assessed jointly.

325   The procedure proposed combines use of strain gauges and microscopic techniques in order to
326   obtain information about the circumferential hoop strains generated during the corrosion process.
327   The circumferential strain is obtained by means of the experimental measurements obtained from the
328   strain gauges and the radial displacements obtained from the wavelength dispersive X-ray
329   spectroscopy (WDS) curves that show the growth of the rust layer.
330   Once the corrosion process has started, three distinct radii may be distinguished: r_0 is the initial
331   radius of the steel bar; r_1 is the radius of the non-corroded steel bar; and r_2 is the total radius of the
332   corroded steel bar, including CL and CAR. According to the geometrical description of these
333   radiuses, shown in Figure 12, Eq. 2 is obtained:

$$r_2 = r_0 + \Delta R \tag{2}$$

335   In addition, the CAR + CL is expressed in this work as:

$$CAR + CL = r_2\text{-}r_1 = \Delta R^* \tag{3}$$

337   and ΔR^* corresponds to the green area shown in Figure 7 and Figure 8.
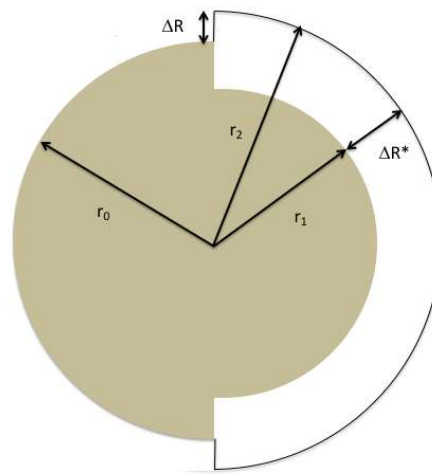
Figure 12. Geometrical considerations of the corrosion process in the reinforcement bar.

340   With the aim of comparing the experimental circumferential strain measured by the strain
341   gauges placed as closely as possible to the steel bar with the analytical modelling, the geometrical
342   dimensions of the strain gauges should be considered. Therefore, another radius is defined by adding
343   the radius of the rebar with the half of the width of a strain gauge (Eq.4), due to it being in contact to
344   the surface of the steel [15].

$$r^* = r_0 + \frac{1}{2}e \tag{4}$$

346   with *r** being the radius the radius of the strain gauge measurement and e the breadth of the
347   strain gauge.
348   It should be noted that the entire corrosion layer thickness indicated in the WDS images,
349   ΔR^*cannot be directly used for the evaluation of circumferential hoop strain, since it includes the
350   CAR. In order to relate the value of $\Delta R^*$with the effective radial displacement obtained ($\Delta R_{effective}$)
351   from the strain gauges measurements, a reduction factor f is proposed [15]. Thus, the effective radial
352   displacement is obtained by adding a reduction factor f in the elastic regime (n = 0).

$$\Delta R_{\text{effective}} = \Delta R^* f \tag{5}$$

354   Subsequently the circumferential strain (Eq. 1), before the opening of the crack or cracks
355   becomes:

356

$$\frac{(\Delta R * f)}{r *} + \frac{\overbrace{wn}^{w=0}}{2\pi r *} = \varepsilon = \varepsilon_{sg}$$

(6)

357   where r^* the radius of the strain gauge measurement, ΔR^* is CL+CAR, f is the reduction factor,
358   w is the width of crack, n is the number of cracks, ε is the circumferential strain that includes the
359   opening of the cracks. Before the opening of the crack or cracks, the value of ε is the measurement
360   assessed by the strain gauges (ε_{sg}).
361   The reduction factor can be obtained from Equation 6. Table 8 and Table 9 show the reduction
362   factor calculated for each concrete mixture at each age studied. The average reduction factor is 0.114
363   for CC, which is slightly higher than the value obtained for SFC, 0.109. Therefore, it could be said that
364   a pore refinement might influence in the decrease of the reduction factor, as in the case of SFC. By
365   contrast, the current intensity does not appear to have significant influence in the reduction factor
366   value in the cases studied.

367   **Table 8.** Relation between the calculated circumferential stress ($\sigma*$) and the ΔR^*, radius in the
368   conventional concrete.

Days	CC50			CC100		
	σ*	CL+CAR (μm)	f	σ*	CL+CAR (μm)	f
2	0	0	0	0	20	0.133
5	2.09	4	0.112	18.89	35	0.115
8	9.17	18	0.109	29.41	65	0.097
14	21.12	43	0.105	72.26	130	0.119
26	78.73	125	0.125	94.13	180	0.112
35	93.53	170	0.118	115.87	225	0.110
Average			0.114			0.114

369   **Table 9.** Relation between the calculated circumferential stress ($\sigma*$) and the ΔR^*, radius in in the
370   concrete with silica fume.

Days	SFC50			SFC100		
	σ*	CL+CAR (μm)	f	σ*	CL+CAR (μm)	f
2	0	0	0	0	0	0
5	0	5	0	24.38	18	0.145
8	4.88	7	0.100	43.03	42	0.110
14	18.66	22	0.121	73.20	85	0.104
26	54.56	72	0.108	162.23	215	0.099
35	86.35	115	0.107	175.12	255	0.087
Average			0.109			0.109

371
372   In order to study the evolution of the crack width with time once the cracks initiate, the average
373   reduction factor obtained from Equation 7 can be used at the ages studied. Table 8 shows the crack
374   widths in all cases according to Eq. 7. Appendix 1 shows the cracks surrounding the rebars of the
375   specimens at several ages of testing. At the moment of crack initiation, some of the strain gauges were
376   broken and crossed by a crack trajectory, though the rest of strain gauges continued measuring
377   circumferential strain. As shown in Figure 3, there were four strain gauges that covered the potential
378   directions of the radial cracks except those that crossed the contact between each pair of strain gauges.
379   In such a way, the detection of the radial crack nucleation could be assured by means of the breakage
380   of any of the strain gauges. Additionally, a slight fall in the strain measured by the unbroken strain
381   gauges is observed at the moment of cracking (see Figure 10). Once the test was completed, prismatic
382   samples of 28x28x5 mm³ with the rebar at the centre were cut in order to observe the amount and the
383   trajectories of cracks. The number of cracks in the specimens was from one to three. The experimental

384   tensile strength was 4.98 MPa for CC and 4.03 MPa for SFC, so the crack width will appear when this
385   tensile ($\sigma*$) is exceeded.

386

$$w = \left(\varepsilon_{sg} - \frac{\Delta R^* f}{r^*} \right) \frac{2\pi r^*}{n} \qquad (7)$$

387   **Table 10.** Cracks widths of the concretes according Equation 7.

Age (days)	CC50 (f=0.114)			CC100 (f=0.119)			SFC50 (f=0.087)			SFC100 (f=0.109)		
	n	$\sigma*$	w (mm)	n	$\sigma*$	w (mm)	n	$\sigma*$	w (mm)	n	$\sigma*$	w (mm)
02	0	0.00	0	0	0.00	0.010	0	0.00	0	0	0.00	0
05	0	2.09	0	1	18.89	0.016	0	0.00	0	1	24.38	0.017
08	1	9.17	0.008	2	29.41	0.054	1	3.72	0.001	1	43.03	0.019
14	1	21.12	0.017	2	72.26	0.144	2	14.16	0.013	2	73.20	0.061
26	3	78.73	0.240	2	94.13	0.174	3	41.39	0.12	2	162.23	0.123
35	3	93.53	0.264	3	115.87	0.310	3	65.52	0.20	3	175.12	0.146

388
389   From the results shown in Table 8, it is worth noting that the use of different current intensities
390 has a direct influence on the day at which the first crack appears. The crack initiation occurs at five
391 days for 50μA/cm2 and eight days for 100μA/cm2 in each concrete, though with a different tensile
392 ($\sigma*$) due to the microstructure of the network.
393   As Figure 13 shows, the pore refinement and current intensity might have a significant influence
394 in the crack width obtained as a function of the electric charge applied. From the beginning of the test
395 to around 750 C, the factor with the greater influence was the current density. The lowest current
396 density applied, 50μA/cm², caused the smallest crack widths in both concrete types, with them being
397 even smaller for SFC50 in comparison with CC50. Above 750 C the crack opening evolution obtained
398 exhibited an increasing dependency on the pore refinement, with the crack widths obtained for the
399 concrete with silica fume, SFC, being significantly lower in comparison with the plain concrete, CC.
400 Additionally, it is worth noting that there is a value of the electric charge, around 1200 C for CC and
401 1800 for SFC, from which the use of the lowest current density caused a higher crack width in
402 comparison with the specimens subjected to the highest current density, 100μA/cm².

403
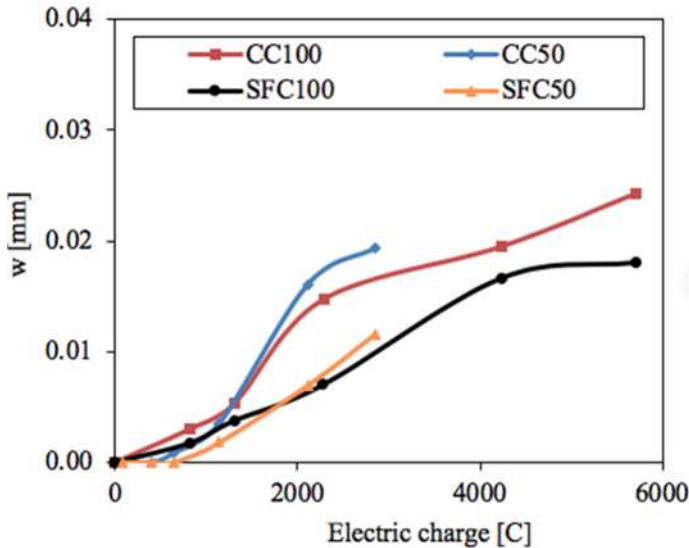
404   **Figure 13.** Evolution of the crack width as a function of the electric charge for each specimen at 50 and
405   100μA/cm².

406   **5. Conclusions**

407   This paper has studied the influence of the porous microstructure and current density in the
408 initiation stage of rebar corrosion process, and the crack formation induced by chloride penetration
409 in concrete.

410   It is shown that the increase in the current density has produced a more rapid development of
411 the corrosion process. Furthermore, it should be noted that the smaller average pore diameter size of
412 the porous microstructure causes a lower capability to accommodate the corrosion products of the
413 concrete, leading to greater circumferential deformations than other cases from very early ages.

414   The combination of an SEM analysis and strain gauges has shown a good performance when
415 studying corrosion development at early ages. The use of wavelength dispersive X-ray spectroscopy
416 allows information about rust growth to be obtained. The experimental work has shown the
417 formation of a rust layer at the interface in a first stage of the corrosion process, which later penetrates
418 through the porous microstructure of the concrete around the steel bar. From the experimental
419 results, an approximately linear relation of steel corrosion product thickness with time is deduced.

420   An analytical model based has been used to reproduce the experimental results. A good level of
421 agreement has been found among the SEM observations, EDS analysis and the strain gauge
422 measurements when a reduction factor f was included in the model for the prediction of the crack
423 width. On the basis of calculations, it could be said that a pore refinement might influence the
424 decrease of the reduction factor, consistent with a lesser capability to accommodate corrosion
425 product.

426   The results obtained showed that embedding the strain gauges in the concrete, placed as closely
427 as possible to the steel rebar, provides more detailed data of the circumferential strain in the concrete
428 than use of strain gauges on the concrete surface. This procedure shows improvement in the cracking
429 models. Therefore, the crack initiation time could be estimated from converting the retrieved strain
430 data into stresses and by comparing them with the tensile strength.

431   In addition, from the results obtained it could be said that the pore refinement and current
432 intensity might have a significant influence on the crack width obtained as a function of the electric
433 charge applied. At very early ages, up to approximately 750 C, the lowest current density applied
434 caused the smallest crack widths in each concrete types. Later, the crack opening evolution obtained
435 exhibits an increasing dependency on the pore refinement, with the crack widths obtained for the
436 concrete with silica fume in comparison with the concrete without additions being significantly
437 lower. Lastly, a value of the electric charge of around 1200 C for the plain concrete and 1800 C for the
438 concrete with silica fume is shown, from which use of the lowest current density causes a higher crack
439 width in comparison with the specimens subjected to the highest current density.

443 **Author Contributions:** The individual contributions are: conceptualization, J. C. Gálvez and E. Reyes;
444 methodology, J. C. Gálvez and E. Reyes; validation, A.M. Bazán; investigation, all authors; resources, J. C.
445 Gálvez;; writing—original draft preparation, SA.M. Bazán and E. Reyes.; writing—review and editing, J.C.
446 Gálvez and E. Reyes; visualization, all co-authors; supervision, J. C. Gálvez and E. Reyes; project administration,
447 J.C. Gálvez; funding acquisition, J.C. Gálvez.

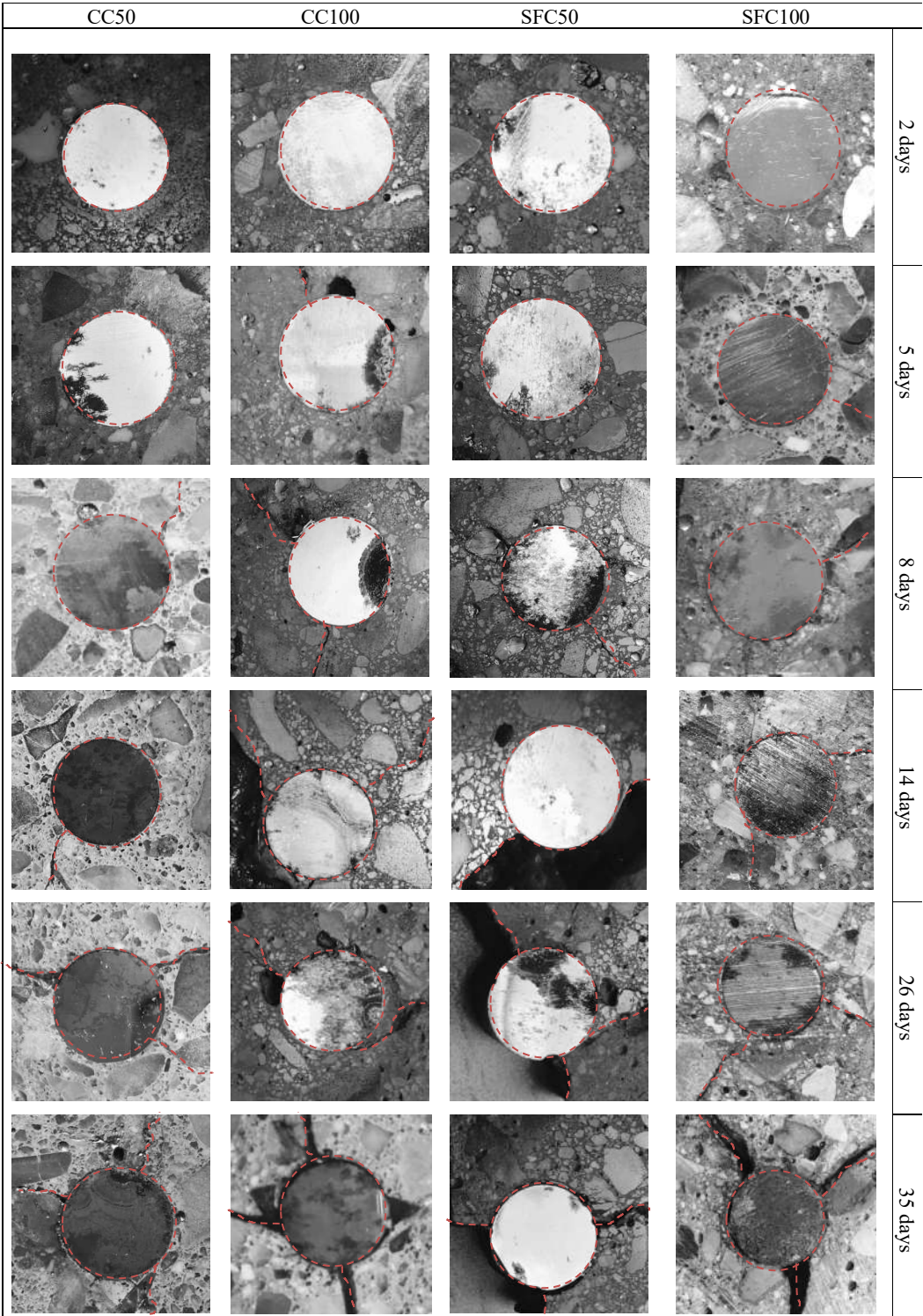448 **Conflicts of Interest:** The authors declare no conflict of interest.

References

450 1.   Cady, P., & Weyers, R. (1983). Chloride Penetration and Deterioration of Concrete Bridge Decks. Cement,
451   Concrete & Aggregate , vol. 5, 2, pp. 81-87.

452 2.   K. Tuutti, Corrosion of steel in concrete., 1982.

453 3.   Zhao, Y., Yu, J., Hu, B., & Jin, W. (2011). Damage analysis and cracking model of reinforced concrete
454   structures with rebar corrosion. Corrosion Science , 53, pp. 3388–3397.

455 4.   Michel A., Pease B.J, Peterová A., Geiker MR, Stang H, Thybo A.E.A. (2014). Penetration of corrosion
456   products and corrosion-induced cracking in reinforced concrete materials: experimental investigations and
457   numerical simulations, Cement and Concrete Composites, 47, pp. 75-86

458 5.   Liu Y, Weyers RE. Modeling the time-to-corrosion cracking in chloride contaminated reinforced concrete.
459   ACI Mater J 1998;95(6):675–81.

6. Val, D., Chernin, L., & Stewart, M. (2009). Experimental and Numerical Investigation of Corrosion-Induced Cover Cracking in Reinforced Structures. Journal of Structural Engineering , 135, pp. 376-385.

7. H.S.Wong, Y.X.Zhao, A.R.Karimia, N.R.Buenfeld, W.L.Jin, (2010), On the penetration of corrosion products from reinforcing steel into concrete due to chloride-induced corrosion, Corrosion Science, 52 (7), 2469-2480.

8. Michel A, Pease BJ, Geiker MR, Stang H, Olesen JF (2011) Monitoring reinforcement corrosion and corrosion-induced cracking using non-destructive X-ray attenuation measurements. Cement and Concrete Research 41:1085–1094.

9. Zhao, Y., Ren, H., Dai, H., Jin, W. Composition and expansion coefficient of rust based on X-ray diffraction and thermal analysis, Corrosion Science, 53 (5), 2011, 1646-1658.

10. Zhao, Y., Yu, J., & Jin, W. (2011). Damage analysis and cracking model of reinforced concrete structures with rebar corrosion. Corrosion science , 53, pp. 3388-3397.

11. Su, R.K.L., Zhang, Y. A double-cylinder model incorporating confinement effects for the analysis of corrosion-caused cover cracking in reinforced concrete structures, 2015, Corrosion Science, 99, pp. 205-218.

12. Batis, G., & Routoulas, T. (1999). Steel rebars corrosion investigation with strain gauges. Cement & Concrete Composites , 21, pp. 163-171.

13. Pedrosa, F., Andrade, C., (2017), Corrosion induced cracking: Effect of different corrosion rates on crack width evolution, Construction and Building Materials 133, pp. 525-533.

14. Zhao, Y., Yu, J., Hu, B., & Jin, W., (2012). Crack shape and rust distribution in corrosion-induced cracking concrete. Corrosion Science , 55, pp. 385-393.

15. A.M. Bazán, J.C. Gálvez, E. Reyes, D. Galé-Lamuela (2018),Study of the rust penetration and circumferential stresses in reinforced concrete at early stages of an accelerated corrosion test by means of combined SEM, EDS and strain gauge, Construction and Building Materials, 184, 655-667.

16. Caré, S., & Raharinaivo, A. (2007). Influence of impressed current on the initiation of damage in reinforced mortar due to corrosion of embedded steel. Cement and Concrete Research , 37, pp.1598-1612.

17. El Maaddaway, T., & Soudki , K. (2003). Effectiveness of impressed current technique to simulate corrosion of steel reinforcement in concrete. Journal of Materials in Civil Engineering , 15, pp.41-47.

18. El-Hadi, Z., Tantawi, N., & Selim, I. (2002). Influence of Silica Fume on Corrosion Behaviour of Reinforced Steel in Different Media. Journal of Material Science & Technology , 18 (1), pp.83-88.

19. Andrade , C., Alonso, C., & Molina, F. (1993). Cover cracking as a function of bar corrosion: Part I-Experimental test. Materials and Structures , 26, pp.453-464.

20. Caré, S., Nguyen, Q.T., L'Hostis, V., Berthaud, Y., (2008) Mechanical properties of the rust layer induced by impressed current method in reinforced mortar, Cement and Concrete Research 38(8-9), pp. 1079-1091

21. N. Yüzer, F. Aköz, and N. Kabay, "Prediction of time to crack initiation in reinforced concrete exposed to chloride.," Construction and Building Materials, 22(6), 1100-1107., 2008.

22. Rouquerol, J.; Avnir, D.; Fairbridge, C. W.; Everett, D. H.; Haynes, J. M.; Pernicone, N.; Ramsay, J. D. F.; Sing, K. S. W.; Unger, K. K. (1994). "Recommendations for the characterization of porous solids (Technical Report)". Pure and Applied Chemistry. 66 (8): 1739–1758. doi:10.1351/pac199466081739

23. Zhao, YX, Dong, JF, Wu, YY and Jin, WL (2016). Corrosion-induced concrete cracking model considering corrosion product-filled paste at the concrete/steel interface. Construction and Building Materials, 116, pp. 273-280.

24. Zhao, YX, Ding, HJ, Jin, WL (2014). Development of the corrosion-filled paste and corrosion layer at the steel/concrete interface . Corrosion Science, 87, pp. 199-210.

25. Timoshenko, S., Goodier, J.N. Theory of elasticity, McGraw-Hill (1969)

26. J.A. Den Uijl, A.J. Bigaj, A bond model for ribbed bars based on concrete confinement. HERON-ENGLISH EDITION-, 41, pp. 201–226.

27. Zhao, Wu, and Jin, "Distribution of millscale on corroded steel bars and penetration of steel corrosion products in concrete," Corrosion Science 66, pp. 160-168, 2013.

508   **Appendix 1.** Crack mapping of CC50, CC100, SFC50 and SFC 100 at 2, 5, 8, 14 26 and 35 days of testing
509   age.

510